PAPER

Check for updates

Magnetic recyclable CoFe$_2$O$_4$@PPy prepared by *in situ* Fenton oxidization polymerization with advanced photo-Fenton performance†

Yuanming Deng, [ID] * Xiaoman Zhao, [ID] Junxuan Luo, Zhong Wang and Jiaoning Tang [ID]

Here we present a magnetic recyclable photo-Fenton catalyst CoFe$_2$O$_4$@PPy with uniform morphology and excellent dispersibility prepared *via* simple *in situ* Fenton oxidization polymerization. The CoFe$_2$O$_4$ core provides good magnetic recyclability for the catalysts as well as the ion source for catalyzed decomposition of H$_2$O$_2$ in PPy coating. The optimal catalytic effect can be obtained by adjusting the ratio of CoFe$_2$O$_4$ and PPy. Methylene blue, Methyl orange and Rhodamine B (RhB) employed as model pollutants certificated that the catalyst exhibits a wide range of photodegradability. The decoloration rates reach nearly 100% in the photodegradation of 10 mg L^{-1} RhB after 2 h visible-light irradiation and only low toxicity small molecules are detected by LC-MS. Moreover, the catalytic activity remains after 5 cycles with decoloration rates up to 90%. The degradation measurement in the presence of scavengers of reactive species reveals that the positive holes (h$^+$) and hydroxyl radical (·OH) are the main reactive oxygen species in the CoFe$_2$O$_4$@PPy system. The performance enhancement may be attributed to the combination of improved Fenton activity by coordinated Fe^{2+} and PPy redox pairs and photo-catalytic activity by broaden adsorption and photo-generated charge separation.

Introduction

Nowadays, organic pigments and dyes are increasingly popular because of the booming chemical industry and the pursuit of better life. The discharge of waste water containing such organic pigments and dyes brings about enormous threats to our environment and health. As an advanced oxidation process, the Fenton reaction has advantages of complete degradation and mineralization of organic pollutants by *in situ* generated highly oxidative free hydroxyl radicals. However, the traditional Fenton reaction encounters problems such as low pH conditions, sluggish Fe^{3+} reduction kinetics and secondary pollutants caused by mass production of slurry containing Fe^{3+}. Therefore, heterogeneous Fenton systems[1–3] in which Fe^{2+} of the catalyst was replaced by Fe(II) active sites from solid iron metals,[4] alloys,[5–7] oxides[7–9] and other compounds are developed for better recyclability. Nevertheless, the rapid re-generation of Fe(II) active site from Fe(III) on the surface of heterogeneous Fenton catalysts remains challenges. Photo-Fenton[10–12] in which the solar energy is utilized to drive the reduction is a promising route to conquer the sluggish kinetic. After the excitation of semi-conductors with photo-catalytic activity, photo-generated electrons on conductive band play a role of reductant for Fe(III) while the photo-generated holes play a role of additional oxidant for organic pollutant.

Transition mixed metal oxide, CoFe$_2$O$_4$, with spinel structure[13] is regarded as one of effective heterogeneous photo-Fenton catalysts along with magnetic recyclability[14,15] as well as unique electrical properties,[16] physicochemical stability,[17] abundant resources, and eco-friendliness.[18] However, poor electron transfer activity and dispersibility severely limit the catalytic activity of the ferrite.[19] Therefore, it is of particular importance to transform the steric hindrance and electrical conductivity of the nanomaterial by changing the surface of the nanomaterial and appropriate doping, thereby obtaining stable nanoparticles and facilitating electron conduction.[20] Coating ferrite with inorganic layers *e.g.* silica,[10,21] inhibits the agglomeration of magnets, thus improves its dispersibility. Modifying ferrite with metal nanoparticles acting as electron acceptors such as Ag,[22] Au,[23] Pd,[24] Cu[25] *etc.* on the surface enhances the separation of photo-generated electron–hole pairs. Carbon nanotubes,[26] graphene,[27,28] C$_3$N$_4$ (ref. 29 and 30) or other organic semiconductors decorated on ferrite, on the one hand, can act as a collector and transmitter of excited electrons because of its conjugated large Π bond, on the other hand, can improve the light absorption, thus enhance the

Shenzhen Key Laboratory of Polymer Science and Technology, Guangdong Research Center for Interfacial Engineering of Functional Materials, College of Materials Science and Engineering, Shenzhen University, Shenzhen 518060, China. E-mail: ymdeng@szu.edu.cn

photo-catalytic activity. In recent years, thanks to the high carrier mobility and chemical stability, conductive polymers such as polythiophene (PTH),[31] polyaniline (PANI),[32,33] polypyrrole (PPy),[34,35] *etc.* are used to modify the ferrite, giving the composites good electron transport capability in photo-catalysis process.[36] The synergistic effect is revealed by the combination of the organic phase and the inorganic phase, as improved photo-catalytic performance compared to each single component is exhibited due to better electron transfer ability through multiple redox pairs.

So far, PPy has been confirmed to effectively enhance the photocatalytic performance of semiconductor photo-catalysts,[37] such as BiOI@PPy,[38] TiO$_2$@PPy,[39] Fe$_3$O$_4$@PPy,[40] *etc.* Moreover, Yu *et al.*[41] found that PPy showed better enzyme-mimic activity than that of horseradish peroxidase (HRP) in catalyzing the decomposition of hydrogen peroxide. Yang *et al.*[42] also tried to combine Fe$_3$O$_4$ with PPy to prepare a peroxide nanozyme with magnetic properties and excellent conductivity. It is deduced that the enzyme-mimic activity similar with Fenton catalytic ability may be related to its porphyrin-like structure. Accordingly, combination of PPy and ferrites may provide novel catalysts with enhanced performance in photo-Fenton degradation of organic pollutants due to their improved dispersibility, recyclability, light-absorption, and electron transfer. However, so far as we know, there are few reports on the application of such kind of catalysts.

Herein, we present a facile preparation of an effective photo-Fenton catalyst with good recyclability and reusability. The PPy coated CoFe$_2$O$_4$ microspheres (CoFe$_2$O$_4$@PPy) were prepared *via* Fenton oxidation induced *in situ* polymerization coating method. In brief, *in situ* generated Fe^{3+} and Co^{2+} by dissolution of CoFe$_2$O$_4$ in acidic solution were used to catalyze the decomposition of H$_2$O$_2$ for the oxidation polymerization of PPy. The coating of PPy on the surface of CoFe$_2$O$_4$ produces a ferromagnetic CoFe$_2$O$_4$@PPy with uniform morphology, good dispersibility and recyclability. The catalyst shows enhanced photo-Fenton activity in the removal of model water pollutants RhB under neutral condition with 95% de-coloration within 30 min irradiation in the presence of 45 mM H$_2$O$_2$. The catalytic activity remains 90% of de-coloration rate after 5 cycles of degradation, revealing good reusability. The degradation of the two dyes, methylene blue and methyl orange, demonstrates the lower selectivity of catalysts.

Results and discussion

The schematic illustration of preparation procedure and principle is shown in Scheme 1. By adding hydrochloric acid to the reaction system, an acidic environment is created and partial of CoFe$_2$O$_4$ is dissolved. The released Fe^{3+} was reduced to Fe^{2+} by pyrrole and the polymerization is initiated. As soon as the addition of hydrogen peroxide, it reacted with the resulted Fe^{2+} to generate a hydroxyl radical in Fenton mechanism, which act as oxidant together with Fe^{3+} to oxidize the pyrrole to form a polypyrrole shell on the surface of CoFe$_2$O$_4$. The presence of small amount of surfactant SDS in the solution is expected to
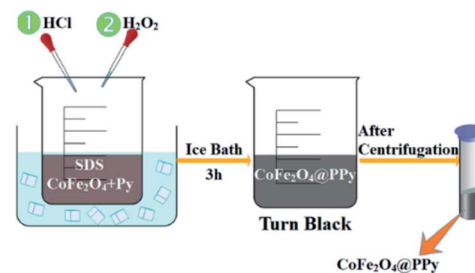
Scheme 1 Schematic illustration for the synthesis procedure of CoFe$_2$O$_4$@PPy.

prevent the agglomeration between polypyrrole coated ferrite microspheres. Therefore, a well dispersed, spherical core–shell structure with uniform particle size distribution was prepared successfully.

Characterization of the catalyst

The amount of Py used for coating is varied as 2 mmol, 4 mmol, 6 mmol and 8 mmol. Accordingly, the obtained CoFe$_2$O$_4$@PPy were named as S1, S2, S3 and S4. The morphologies of synthesized catalysts S1, S2 and S3 characterized by SEM and TEM were shown in Fig. 1a–c. It can be seen from Fig. 1 that the prepared CoFe$_2$O$_4$@PPy exhibits spherical morphology with diameter of 200 nm on average and excellent dispersibility. With the increase of PPy content, the size of CoFe$_2$O$_4$@PPy microspheres hardly increases but their surface becomes increasingly rougher than that of pure CoFe$_2$O$_4$ (Fig. S1†), revealing that the surface of CoFe$_2$O$_4$ is coated with a very thin layer of PPy. However, there's no obvious PPy layer can be resolved from TEM images as shown in Fig. 1 when the PPy dosage no more than 6 mmol, implying the PPy layer on S1, S2 and S3 is too thin. Legible PPy coating layer is observed for S4 when the dosage of Py is up to 8 mmol. From the TEM as shown in the inset of Fig. 2a, a boundary between PPy and CoFe$_2$O$_4$ is appeared vividly. The magnified TEM image of S4 as shown in Fig. 2b indicates that the surface of CoFe$_2$O$_4$ microspheres was covered with an amorphous layer of about 10 nm thickness. To get a deep insight on the structure of S4, high resolution TEM and selected area electron diffraction (SAED) measurements were performed. The SAED pattern as shown in Fig. 2c shows a series of discontinuous diffraction rings with inter-planar distance of 0.299, 0.254, 0.174, 0.166 and 0.150 nm which are corresponding to the distance between crystal planes of {220},
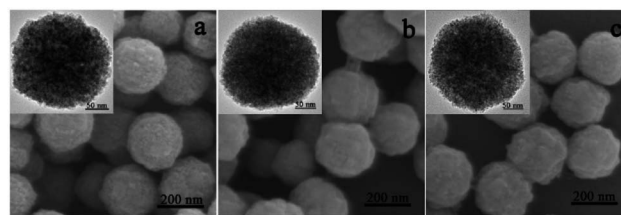

Fig. 1 SEM images of S1 (a); S2 (b); S3 (c). Insets are TEM images corresponding to the SEM, respectively.
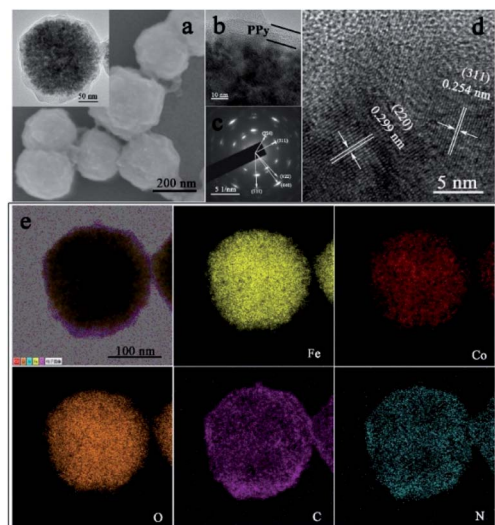
Fig. 2 The SEM image of S4 (a); the TEM image of S4 (b); the SAED pattern of S4 (c); the HRTEM image of S4 (d); the TEM-EDS image of S4 (e).

{311}, {422}, {511} and {440}, revealing a polycrystalline with cubic lattice structure of CoFe$_2$O$_4$ microspheres. From HRTEM image of Fig. 2d, the inter-planar distance is calculated to be 0.299 and 0.254 nm, corresponding to (220) and (311) plane of CoFe$_2$O$_4$ respectively. Furthermore, the EDS mapping of a single microsphere of S4 as shown in Fig. 4e clearly signifies that CoFe$_2$O$_4$@PPy contains five elements of Co, Fe, O, C and N, among which C and N elements evenly distributed on the

surface of CoFe$_2$O$_4$, demonstrating that PPy is successfully coated on CoFe$_2$O$_4$ microspheres.

The XRD patterns of original CoFe$_2$O$_4$, PPy and CoFe$_2$O$_4$@PPy loaded with different content of PPy are depicted in Fig. 3a. The diffraction peaks at 2θ values of 30.084°, 35.437°, 43.058°, 53.445°, 56.973°, 62.585°, and 74.009° correspond to the standard peak positions of spinel CoFe$_2$O$_4$ structure (PDF no. 22-1086). However, the pattern of PPy has only one broaden diffraction peak with a 2θ value of 26° due to the amorphous structure of PPy polymer. The patterns of CoFe$_2$O$_4$@PPy have no obvious PPy diffraction peak but strong diffraction signal of CoFe$_2$O$_4$, which is attributed to the strong signal of CoFe$_2$O$_4$ tending to overwhelm the weak carbon peak. Thermogravimetric analysis (TGA) in air was also carried out for further confirming the existence of PPy and roughly estimating its amount. Due to the weight loss caused by the volatilization of adsorbed water is observed at around 100 °C, the thermo-gravimetric analysis is started from 100 °C. The temperature was raised from 100 °C to 800 °C for the pyrolysis of PPy.[43] As shown in Fig. 3b, PPy is almost completely oxidized at 650 °C and the weight loss is near 100%, whereas the curve for CoFe$_2$O$_4$ only shows a slight weight loss (~5%) at 600 °C. The weight loss for the composites consecutively increases with the increase of the PPy content. From the weight loss of composites, the content of PPy in S1, S2, S3 and S4 is estimated to be 40, 23, 16 and 11 wt%. The Raman spectra of CoFe$_2$O$_4$@PPy and bare PPy, CoFe$_2$O$_4$ are shown in Fig. 3c. There are two distinct broad peaks ranging from 1200 cm^{-1} to 1800 cm^{-1} in CoFe$_2$O$_4$@PPy and pure PPy. The peak at 1350 cm^{-1} is assigned to the D band (C–N stretching vibration), which mainly due to the presence of structural defects
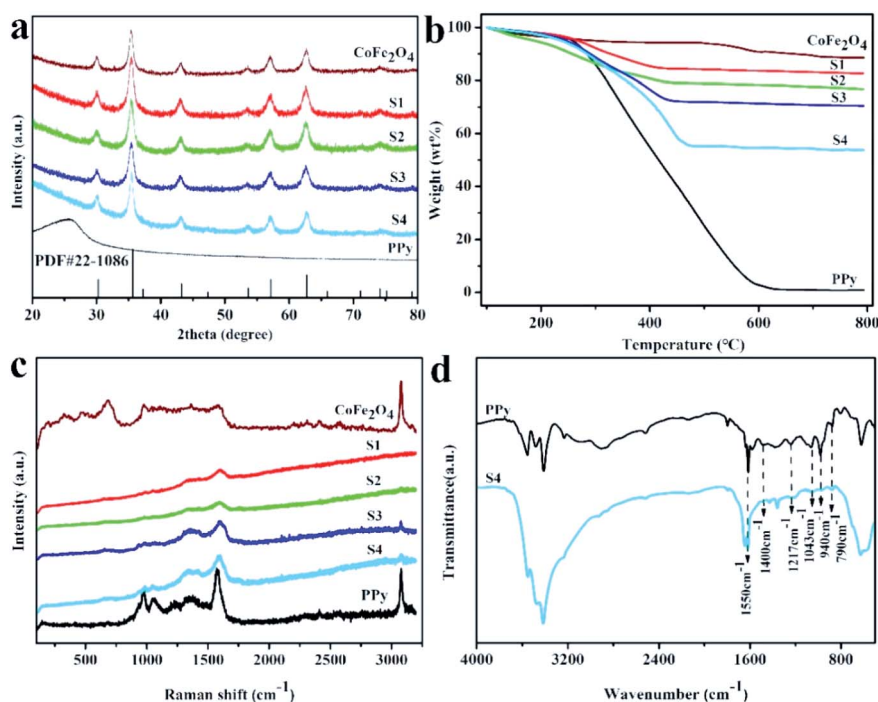

Fig. 3 Powder XRD patterns of PPy, CoFe$_2$O$_4$, and S4 (a); FT-IR spectra of PPy and S4 (b); Raman spectra (c) and TGA patterns (d) of PPy, CoFe$_2$O$_4$, and S4.

and marginal unsaturated carbon, while the characteristic peak at 1580 cm^{-1} is attributed to the G band (C=C stretching vibration), representing the in-plane stretching vibration of carbon atom sp^2 hybrid.[34,44] It can be seen from Fig. 3c that unloaded CoFe$_2$O$_4$ has no obvious G band or D band, whereas there is a significant double peaks after PPy loading, indicating the existence of PPy in the composites. In addition to the existing D band and G band, two peaks at 1045 and 977 cm^{-1} are observed because of the existence of PPy with the polaron (NH$^+$) and bipolaron structures (N$^+$). It is worth noting that after the addition of CoFe$_2$O$_4$ to the PPy matrix, the characteristic absorption peak of PPy at 1579 cm^{-1} was blue-shifted to 1592 cm^{-1}. This transfer may be owing to the interaction between CoFe$_2$O$_4$ and PPy backbones. The pure polypyrrole has a sharp G band and a flat D band, while for CoFe$_2$O$_4$@PPy, the relative intensity of the D band and the G band decreases, manifesting that the degree of disorder of PPy increases due to the introduction of CoFe$_2$O$_4$ nanoparticle.[45] FT-IR measurement was also performed. As shown in Fig. 3d, the absorption peak at 1550 cm^{-1} is attributed to the anti-symmetric stretching of pyrrole ring due to the stretching vibration of the C=C bond; the absorption peaks observed at 1400 and 1043 cm^{-1} correspond to the N–H and C–H deformation vibrations; and the peak at 1217 cm^{-1} is derived from C–N$^+$ stretching,[46,47] moreover 940 cm^{-1} and 790 cm^{-1} are the C–C bond vibration and the out-of-plane vibration of C–H bond,[41] respectively.

The specific surface area and pore size distribution of the samples can be determined by isothermal nitrogen adsorption–desorption curves. The results as shown in Fig. 4a indicate that the curves of CoFe$_2$O$_4$, PPy, CoFe$_2$O$_4$@PPy own hysteresis loop consistent with the IV type adsorption–desorption behavior. The BET surface areas of pure CoFe$_2$O$_4$, PPy, CoFe$_2$O$_4$@PPy calculated by isotherms are 90.48, 8.65, 69.86 cm^2 g^{-1}, respectively. The coating of PPy reduces the specific surface area of CoFe$_2$O$_4$@PPy, which may be attributed to the filling or covering of the micropores of CoFe$_2$O$_4$. CoFe$_2$O$_4$ and CoFe$_2$O$_4$@PPy have a slight capillary condensation step in the relative pressure range of 0.44–0.87, indicating that the material has a large mesopores.[48] In addition, the hysteresis loop in the curve shows high permeability between the mesopores. Fig. 4b shows that the pore size is mainly distributed at 1–20 nm, which suggests that CoFe$_2$O$_4$ and CoFe$_2$O$_4$@PPy are mainly mesoporous structures, giving them physical adsorption capacity.

The valence state and element ratio in CoFe$_2$O$_4$@PPy and CoFe$_2$O$_4$ were analyzed by XPS as shown in Fig. 5. From the full XPS spectra shown in Fig. 5a, the peaks of elements C, O, Fe, Co were observed at nearly 280, 530, 720 and 780 eV successively. Apart from those observed for CoFe$_2$O$_4$, the signal for CoFe$_2$O$_4$@PPy emerged at approximately 400 eV is ascribed to nitrogen element in coated PPy layer. The magnification spectra of signals assigned to specific element C, N, O, Co and Fe were shown in Fig. 5b–f. C 1s XPS spectra in Fig. 5b was fitted by four component peaks at 284.4, 285, 286, and 288.5 eV, corresponding to C–C, C–H, C–N, C=O groups[49] respectively. The main peak at 399.8 eV in the deconvoluted N 1s XPS spectrum (Fig. 5c) is assigned to neutral amine nitrogen(–NH–),[50,51] whereas the small peak at 401.6 eV could be originated from iron–nitrogen related bond (Fe–N type) which is regarded as catalytic active Fe–N sites. The O 1s spectra as shown in Fig. 5d can be divided into several peaks at around 530.36, 531.73 and 533.1 eV, which can be assigned to the surface adsorbed hydroxyl oxygen, water and crystal lattice oxygen O^{2-} (ref. 16) respectively. For CoFe$_2$O$_4$@PPy, the peak locating at 530.36 eV is weakened due to the cover of PPy layer. Notably, an additional peak at 531.1 eV appeared, probably due to the formation of Fe–O–C bond between PPy and Fe^{2+}, which is beneficial for the rapid transfer of electrons during the photo-Fenton reaction.[52] The PPy coating also reduced the relative strength of Fe and Co. From Fig. 5e, the three characteristic peaks with binding energies of 780.05 ± 0.2 eV, 781.89 ± 0.2 eV and 785.9 eV are ascribed to Co 2p$_{3/2}$. The binding energies of 780.05 ± 0.2 eV and 781.89 ± 0.2 eV are Co^{2+} ions at octahedral and tetrahedral positions,[53] respectively, confirming the chemical state as Co(II). The signal at 785.9 eV is characterized to be the satellite peak of Co 2p$_{3/2}$ main line. In the Fe 2p spectrum of CoFe$_2$O$_4$ (Fig. 5f), signals appear at 711.10 and 724.7 eV with the separation of ~13 eV are ascribed as Fe 2p$_{3/2}$ and Fe 2p$_{1/2}$, respectively, indicating the presence of Fe^{3+}. Furthermore, a satellite peak appears at the binding energy of 720.14 eV, which is a typical feature of Fe^{3+}. However, the two significant peak positions of CoFe$_2$O$_4$@PPy shifted to a low binding energy by 1.35 eV with the separation of ~6 eV,[54] demonstrating the existence of Fe^{2+}. The appearance of Fe^{2+} may be due to the reduction of Fe^{3+} by Py during the *in situ* growth of Py and then Fe^{2+} strongly coordinated with the nitrogen atom in PPy,[35] controlled growth of PPy
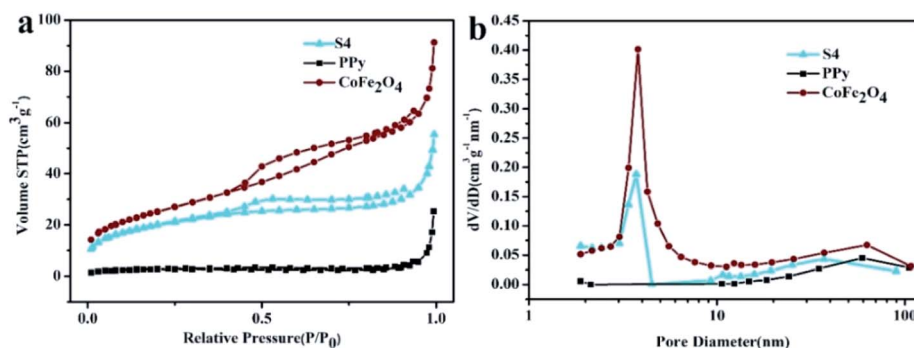

Fig. 4 Nitrogen absorption–desorption isotherms (a) and the pore size distribution curve (b) of pure CoFe$_2$O$_4$, PPy and S4 composite.
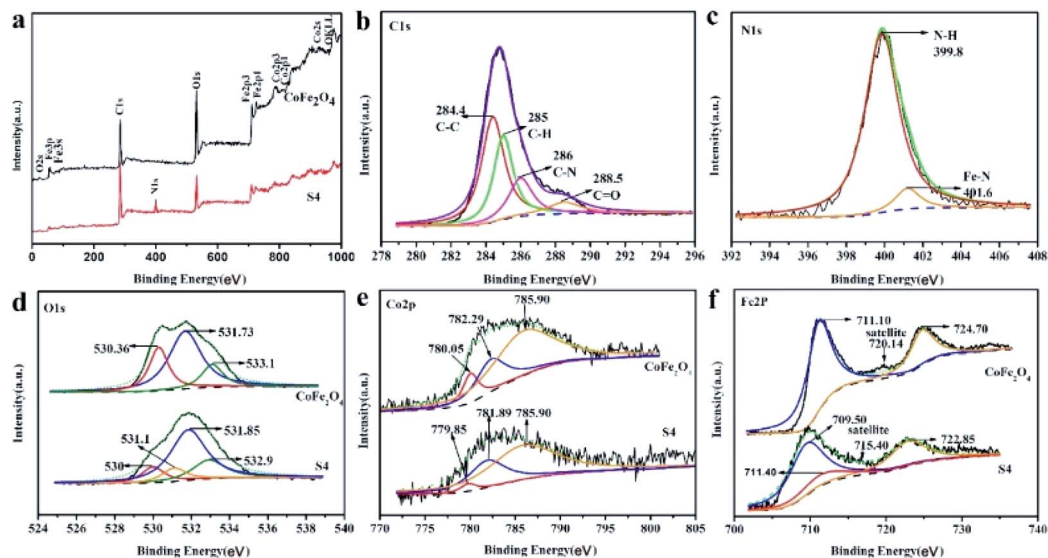
Fig. 5 XPS spectra of the pure $CoFe_2O_4$ and S4. Survey of the samples (a); C 1s narrow scan (b); N 1s narrow scan (c); O 1s narrow scan (d); Co 2p narrow scan (e) and Fe 2p narrow scan (f).

into the surface of $CoFe_2O_4$. Accordingly, Fe^{2+} is embedded in the interior of PPy which is consistent with the result of EDS.

The catalytic activity and reusability of catalysts in Fenton degradation of RhB

The abilities of different samples to degrade organic substance under dark Fenton, photocatalysis, photo-Fenton were detected using RhB as a model pollutant, and the results were shown as

Fig. 6a–c. It can be seen from Fig. 6a that the adsorption of RhB is significantly increased with the incorporation of PPy, which may be attributed to the strong interaction between RhB and PPy. Compared with $CoFe_2O_4$ and PPy, PPy modified $CoFe_2O_4$ showed obvious dark Fenton activity when H_2O_2 was added in, as the concentration of RhB decreased gradually because of the Fenton-like degradation. The improved catalytic performance of $CoFe_2O_4$@PPy and PPy may be attributed to the presence of Fe^{2+}
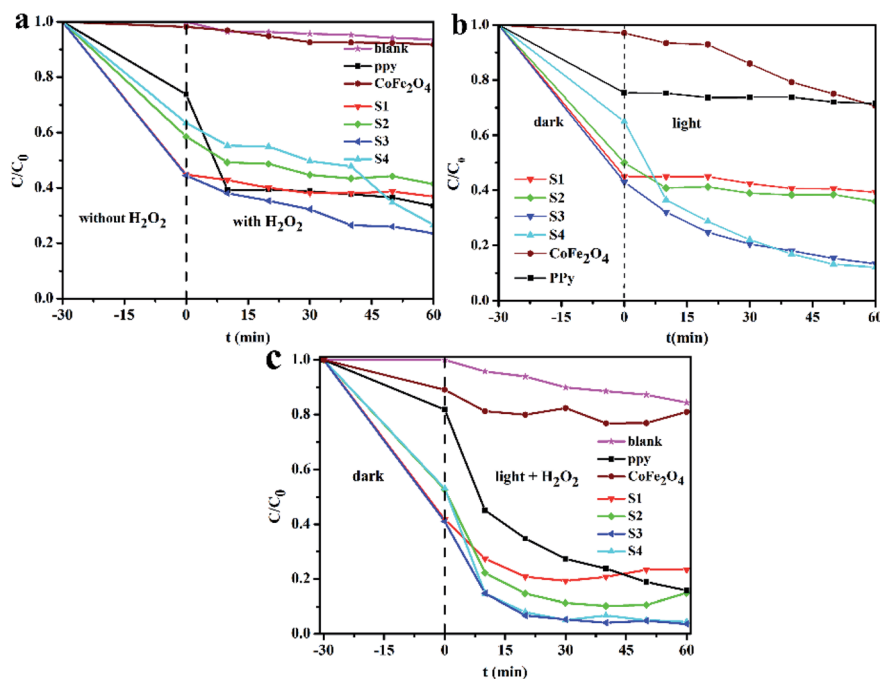

Fig. 6 Rhodamine degradation ability under dark Fenton for all samples (a); the photocatalytic degradation of RhB over all samples under visible light irradiation (b), the photo-Fenton degradation of RhB solution with the presence of H_2O_2 under visible light irradiation (c) ($C_{RhB} = 5$ mg L^{-1}, $C_{H_2O_2} = 45$ mM, pH = 7).

coordinated in PPy, which may be dissolved and released into the solution to catalyze the decomposition of H_2O_2, similar with that reported in the enzyme-mimic behavior. It is worth mentioning that PPy decolorized RhB by 50% in the first 10 minutes of dark Fenton. This may be due to the large amount of Fe^{2+} anchored into PPy during synthesis process. With the addition of H_2O_2 during the dark Fenton process, it is consumed in a short time. Subsequently, the ability of PPy to degrade RhB tends to be gentle, while other composites still maintain a stable activity. Among them, the dark Fenton ability of S1 and S2 is poor, which may be due to the relatively small amount of PPy coating. Although S3 has a higher degree of decoloration at 60 minutes compared with S4, we believe this is mainly due to the strong adsorption effect during dark process. Comparing the dark Fenton activity, S4 has a better catalytic ability, and the photocatalysis is consistent with this result. Fig. 6b shows that the photocatalytic ability of S4 is better than that of S3. This strongly indicates that S4 has improved electron–hole transport ability and more oxidizing substances are generated. The photo-Fenton degradation behavior shows significantly better performance than that of dark Fenton and photocatalysis shown as Fig. 6c. Similarly, the activity of $CoFe_2O_4@PPy$ increases with the increase of polypyrrole
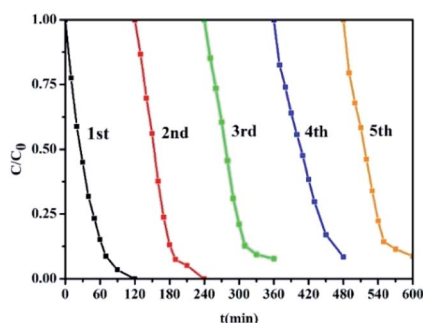

Fig. 7 Cycling runs for the photodegradation of RhB in the presence of S4 under visible light irradiation. ($C_{RhB} = 10$ mg L^{-1}, $C_{H_2O_2} = 45$ mM, pH = 7).

content. Since S4 is the composite with the best synergy effect, we chose S4 as the main research object in subsequent experiments. In order to prove the non-selectivity of catalytic degradation, we also selected methyl orange and methylene blue as substances to be degraded, which showed outstanding photodegradation effect (Fig. S2–S4†).

The reusability of $CoFe_2O_4@PPy$ was investigated by cycling test. To reduce the influence of RhB adsorption in the degradation, the RhB concentration is increased to 10 mg L^{-1} and the time of each cycle is set as 2 h. As shown in Fig. 7, the degradation efficiencies of RhB in these five cycles are 99.7%, 99.5%, 92.1%, 91.4% and 91.2%, respectively. Although the degradation efficiency was slightly reduced, the overall decolorization effect was still significant, demonstrating that the stability of the system is still brilliant. The slight decrease of decolorization rate may be owing to the adsorption of small molecules on the surface of $CoFe_2O_4@PPy$ after decomposition of RhB molecule, occupying the catalytic position on the surface active site. We compare this work with others, as shown in Table 1, which demonstrates that $CoFe_2O_4@PPy$ has better photocatalytic ability.

Degradation pathway and species of RhB

The photo-Fenton degradation mechanism of RhB may be that the RhB molecule is eventually oxidized.[55] As the reaction progressed, the RhB solution decolored from rose red to a colorless chromophore. However, the decolorization of RhB does not mean complete mineralization, and the intermediate products produced during the degradation process may also be contaminated and toxic, and cannot achieve the purpose of our initial preparation of the catalyst. Therefore, during the experiment, we chose to scan a wavelength range of 200–650 nm. Fig. 8a shows that the peak at 553 nm is decreasing, and the peak at 259 nm, 310 nm, and 320 nm gradually disappears, indicating that the aromatic chain, N-position ethyl group and conjugated structure in the RhB molecule are gradually destroyed during the reaction resulting in small organic molecules.[55] Due to the destruction of the C=N and C=O

Table 1 The comparison of this work with others

Catalyst	Dye	Reaction conditions	Degradation	Reusability	Ref.
$CoFe_2O_4@PPy$	RhB	[Dye] = 5 mg L; $[H_2O_2]$ = 45 mM; pH = 7; catalyst = 0.01 g	99.5% (30 min)	5th (90%)	This work
$Fe_3O_4/P(MAA-MBAA)-PPy/Au/void/TiO_2$	RhB	[Dye] = 5 mg L; pH = 3; catalyst = 4 mg	100% (90 min)	6th (70.2%)	62
$Ag@CoFe_2O_4/Fe_2O_3$	RhB	[Dye] = 5 mg L; $[H_2O_2]$ = 225 mM; pH = 7; catalyst = 2 cm × 2 cm square	99.15% (1 h)		63
Reduced graphene oxide-$CoFe_2O_4$	Malachite green	[Dye] = 5×10^{-6} M; $[H_2O_2]$ = 112.5 mM; pH = 7; catalyst = 0.05 g	100% (30 min)		64
rGO/PB/PPy	RhB	[Dye] = 10 mg L; $[H_2O_2]$ = 22.5 mM; pH = 6.18; catalyst = 0.01 g	95.2% (30 min)	4th (91.5%)	65
$rGS/Fe_xO_y/NCL$	RhB	[Dye] = 10 mg L; $[H_2O_2]$ = 180 mM; pH = 7; catalyst = 0.03 g	100% (150 min)	5th (94.6%)	66
PPy NF/Zn–Fe LDH	Safranin	[Dye] = 5 mg L; catalyst = 0.02 g; pH = 7	88% (120 min)	6th (58%)	67

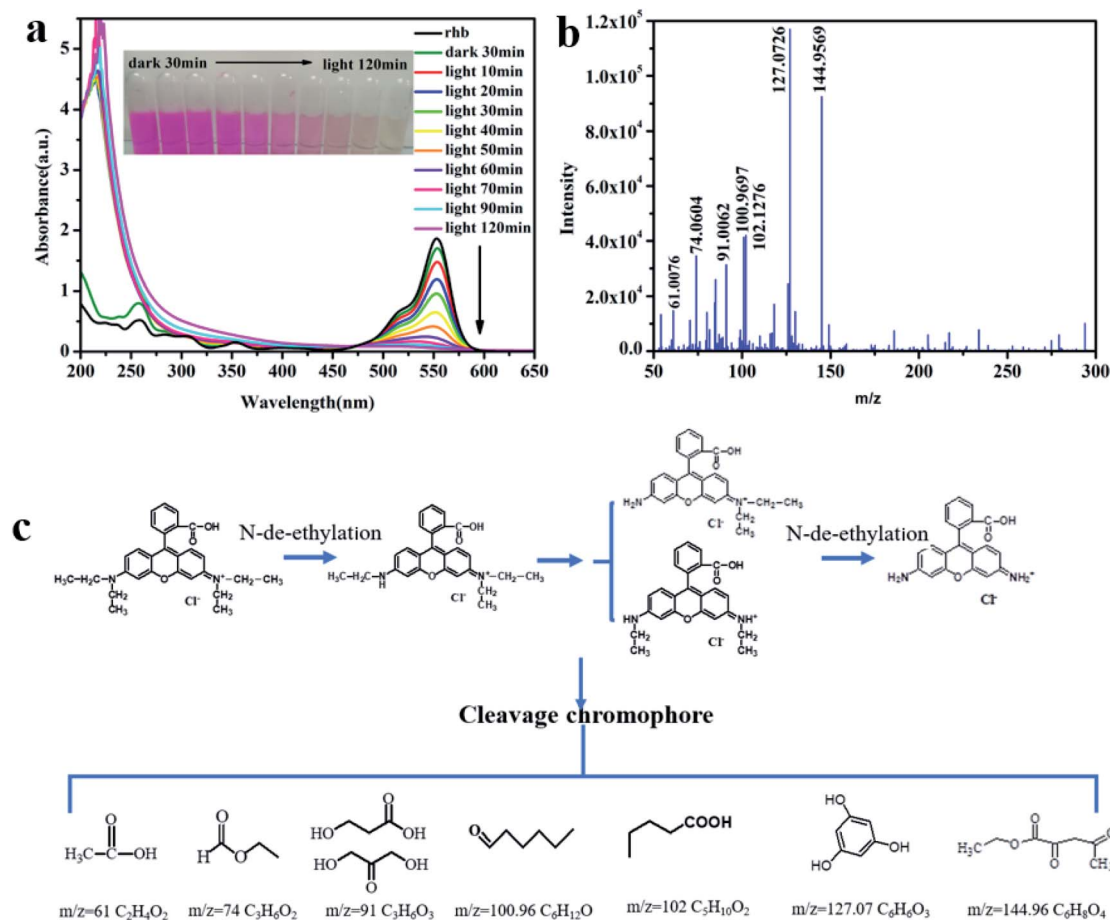**Fig. 8** The photocatalytic degradation of RhB over S4 under visible light irradiation ($C_{RhB} = 10$ mg L^{-1}, $C_{H_2O_2} = 45$ mM, pH = 7) (a). LC/MS spectra of end products of the photo-Fenton degradation of RhB (b), the degradation path of possible intermediates (c).

conjugated structures, the characteristic absorption peak at 553 nm gradually decreases.[56] The disappearance of the absorption peak at 259 nm indicates that the structure of the benzene ring has been destroyed. However, the peak at 225 nm has been rising. It is speculated that the conjugated structure of the RhB molecule is gradually destroyed during the reaction, and other non-polluting small molecules may be formed by de-ethylation at the N-position. In order to gain a deeper under-standing of the colorless products after degradation, we conducted a LC/MS test. After two hours of visible light irradiation, the final colorless product of Rhodamine B degradation was used for LC-MS testing to analyze the components. From Fig. 8b, the final products were mainly small molecule compounds, which means RhB has been completely decomposed into low-toxic or even non-toxic substances. Based on the results of LC-MS, the structures of major intermediates can be inferred as Fig. 8c. The degradation process mainly involves: (i) at the beginning, the peaks differ exactly by 28 mass units successively, indicating sequential N-de-ethylation of RhB. (ii) The intermediate is further broken down into several compounds by the cleavage of the azo (C–N) bond. Fragmented compounds have no chromophore, resulting in colorless. A ring-opening reaction occurs, decomposing the intermediate

into small molecules. Further mineralization into H_2O and CO_2 eventually.

The mechanism in performance enhancement

To deep understand the mechanism in performance enhance-ment, PL tests and quench experiments were conducted. The room temperature PL spectrum was used to study the separa-tion and recombination rate of photoexcited charges of charge carriers. As shown in Fig. 9a, the PL spectrum of CoFe$_2$O$_4$ shows only one emission peak at 427 nm. Whereas, that of CoFe$_2$-O$_4$@PPy shows two emission peaks at 427 nm and 620 nm, which are attributed to the band PL and the exciton PL respectively.[57] Compared to the PL of CoFe$_2$O$_4$, the lower intensity of band PL at 427 nm in PL of CoFe$_2$O$_4$@PPy indicates that the load PPy contributes to the separation of the photo-generated charges, resulting less charge recombination. The incorporation of PPy also introduces in a broad emission peak range from 500 to 750 nm, which can be attributed to the oxygen-related defects (such as oxygen gaps).[58] This observation reveals that the coating of PPy results defect-rich surface and oxygen vacancy of CoFe$_2$O$_4$, which are also evidenced by the XPS results. Quenching experiments were carried out to investigate the active species of photocatalytic properties. In the photo-
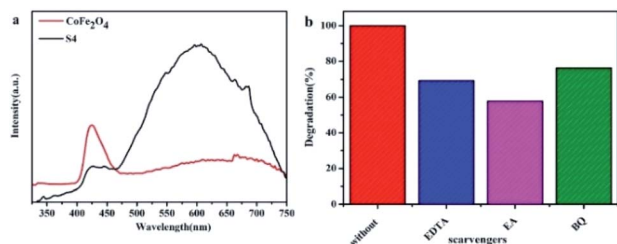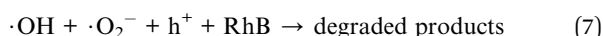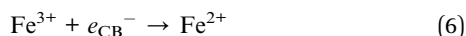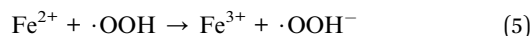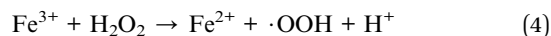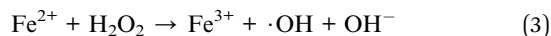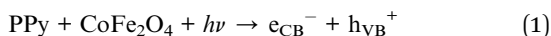
Fig. 9 PL spectra of CoFe$_2$O$_4$ and S4 (a); trapping experiment of active species during the photocatalytic degradation of RhB over S4 under visible light irradiation (b) (C_{RhB} = 10 mg L^{-1}, $C_{H_2O_2}$ = 45 mM, pH = 7).

Fenton process, superoxide radicals from oxygen reduction, photo-generated holes, and hydroxyl radicals from H$_2$O$_2$ decomposition and water oxidation are responsible for the degradation of organic pollutants. Therefore, EDTA as the electron donor, ethanol (EA) containing α-H as the free radical scavenger and benzoquinone (BQ) as the superoxide radical quencher were added into the photo-Fenton system individually. As shown in Fig. 9b, compared with the control experiment without any quencher, the RhB decolorization rate decreased by 57.74%, 69.25% and 76.16% after adding EA, EDTA and BQ respectively, revealing a complicate contribution of decolorization. According to the results of the quenching test, we speculated the mechanism of performance improvement. CoFe$_2$O$_4$ and PPy will generate photo-induced electrons and holes under light irradiation[59] (reaction (1)). Under light irradiation, the photo-generated electrons of CoFe$_2$O$_4$ move to the PPy shell and react with oxygen attached to the surface to generate ·O$_2^-$ (reaction (2)), which contributed to the degradation of organic matter. Simultaneously, Fe^{2+} located between the core and shell can form a Fenton reaction system with H$_2$O$_2$ to form Fe^{3+} (reaction (3)). Hydrogen peroxide can be captured by Fe^{3+}, generating Fe^{2+} and performing Fe^{2+}/Fe^{3+} cycles (reaction (4)–(6)), which makes recycling and stability possible. Moreover, ·OH generated in this process is the most important active species according to the trapping experiment. The accumulated h$^+$ can oxide the organic substrates directly[60] (reaction (7)).

$$PPy + CoFe_2O_4 + h\nu \rightarrow e_{CB}^- + h_{VB}^+ \tag{1}$$

$$O_2 + e_{CB}^- \rightarrow ·O_2^- \tag{2}$$

$$Fe^{2+} + H_2O_2 \rightarrow Fe^{3+} + ·OH + OH^- \tag{3}$$

$$Fe^{3+} + H_2O_2 \rightarrow Fe^{2+} + ·OOH + H^+ \tag{4}$$

$$Fe^{2+} + ·OOH \rightarrow Fe^{3+} + ·OOH^- \tag{5}$$

$$Fe^{3+} + e_{CB}^- \rightarrow Fe^{2+} \tag{6}$$

$$·OH + ·O_2^- + h^+ + RhB \rightarrow degraded\ products \tag{7}$$

Generally, the larger specific surface area can provide more active sites for photodegradation and promote photocatalytic reaction. However, the relatively poor catalytic performance of

CoFe$_2$O$_4$ reveals that the factor response for photo-Fenton activity is far beyond the specific surface area. The quench experiments also indicate that in CoFe$_2$O$_4$@PPy catalyzed photo-Fenton, the contributor on degradation is more than hydroxyl radicals. Therefore, the improvement of degradation performance may be attributed to several factors. Firstly, there is an appropriate amount of Co^{2+}, Fe^{2+} and Fe^{3+} embedded in the interior of PPy during the polymerization, which may accelerate the decomposition of H$_2$O$_2$ through Fenton way, which may mainly contribute to the formation of hydroxyl radicals. Secondly, oxygen vacancy and lattice defect may be introduced into the CoFe$_2$O$_4$ during the PPy coating. The existence of oxygen vacancy enhances the adsorption of substrates, provides more active sites, and promotes the photo-generated charge separation.[61] Thirdly, as an organic semiconductor, PPy not only promotes the light harvesting, but also accelerates electron transfer in the re-generation of active site for Fenton reaction through redox pairs. In summary, the improvement on degradation activity of photo-Fenton can be attributed to the combination of improved Fenton oxidation and additional photo-catalyzed degradation provided by coated PPy layer on CoFe$_2$O$_4$ microspheres.

Experimental

Materials and reagents

CoSO$_4$·7H$_2$O, FeCl$_3$·6H$_2$O, ethylene glycol (EG), pyrrole (Py), rhodamine B (RhB), hydrogen peroxide (H$_2$O$_2$, 30%), hydrochloric acid (HCl) were obtained from Aladdin (China). Sodium dodecyl sulfate (SDS), sodium acetate anhydrous (NaAc, AR), polyethylene glycol (PEG), ethylenediaminetetraacetic acid (EDTA), methanol (MA) and benzoquinone (BQ) were purchased from Macklin (China). All chemicals were used without further purification.

Preparation of CoFe$_2$O$_4$@PPy

CoFe$_2$O$_4$ was prepared according to the previous work,[43,68] and the details are shown in the ESI.† The CoFe$_2$O$_4$@PPy was synthesized via in situ Fenton oxidation polymerization of pyrrole. Typically, 50 mg CoFe$_2$O$_4$, 100 mg SDS and various amounts of pyrroles were mixed with 40 mL water under magnetic stirring to form a homogeneous brown dispersion. To the dispersion cooled under ice bath, 280 μL HCl and 2 mL 30% H$_2$O$_2$ were successively dropped in, and vigorous stirring was continued for other 3 hours. The product was collected by centrifugation and repeated washed, then vacuum dried at 65 °C for 12 h. For comparison, PPy nanoparticles were also prepared according to the previous report. In this synthesis procedure, the molar ratios of CoFe$_2$O$_4$/PPy were adjusted at 1 : 2, 1 : 4, 1 : 6 and 1 : 8, and the corresponding CoFe$_2$O$_4$@PPy samples were named Sx (x = 1–4).

Characterization

The morphology and composition of samples were observed by scanning electron microscope (SEM, SU-70) equipped with EDS and Transmission electron microscope (TEM) (JEM-21200F).

The magnetic properties of $CoFe_2O_4$ and $CoFe_2O_4$@PPy composites were measured in a vibrating sample magnetometer (Quantum Design Corporation, USA) with a maximum applied field of ± 2 T. X-ray diffraction (XRD) curves were recorded with an X-ray diffractometer (Smart Lab) using Cu Kα radiation ($\lambda = 1.5418$ Å). The chemical structure of samples was characterized by FT-IR spectrometer.

(Nicolet 6700) and FT Raman Microscope (RENIDHAW invia). The chemical valence state of samples was analyzed by XPS (PHI5000 Versa Probe II). TGA was performed to understand the content of PPy on a thermal analyzer (TGA 55) at a heating rate of $10°C$ min^{-1} from ambient to 800 °C in air. The nitrogen adsorption desorption isotherms were measured at 77 K using a Micromeritics ASAP 2460 system, and the surface area and pore size distribution were calculated using the Brunauer–Emmett–Teller (BET) and Barrett–Joyner–Halenda (BJH) method, respectively. The UV-Vis absorption spectrum (UV-Vis) was characterized with a UV-Vis spectrometer (PerkinElmer Lambda 950). Liquid chromatography tandem mass spectrometry (LCMS) with QTRAP6500+ was employed to determine the final product of rhodamine decolorization. Photoluminescence (PL) emission spectra was performed on a Renishaw in *via* spectrometer with 285 nm UV light as the excitation source.

Degradation of RhB by heterogeneous catalyst

The photo Fenton activity was assessed by the degradation of rhodamine B (Rh B) under visible light irradiation with a 300 W xenon lamp with a 420 nm cut-off filter. Typically, 10 mg sample was dispersed in 50 mL 10 mg L^{-1} of RhB in a baker with cycling water cooling and magnetic stirring. After 30 min for adsorption in dark, 200 μL of 30% H_2O_2 was added in and light on. Solution was taken out at preset intervals and centrifuged prior to UV-visible spectrometry analysis. The dark Fenton activity was assessed similarly except lighting off. The catalyst after 1 cycle of 2 h degradation test was washed with ethanol and dried thoroughly, then used for the other cycle of degradation to evaluate its reusability. Photo degradation in the presence of ethylene diamine tetra-acetic acid (EDTA), methanol (MA) and benzoquinone (BQ) as a quencher for holes, hydroxyl radicals and superoxide radicals respectively, was also carried out to study the active species during degradation.

Conclusion

In summary, $CoFe_2O_4$@PPy prepared *via* a simple *in situ* Fenton oxidization polymerization coating was applied for the photo-Fenton degradation of organic pollutants. The $CoFe_2O_4$ core in PPy coating provides outstanding magnetic recyclability (Fig. S5†) for the catalysts as well as provides the ion source for catalyzed decomposition of H_2O_2. The prepared $CoFe_2O_4$@PPy exhibited improved performance in Fenton and photo-Fenton degradation of RhB, which was superior to those of pure $CoFe_2O_4$ and PPy. The LC-MS of RhB degradation residues indicates that only low-toxic species are reserved. The possible performance enhancement mechanism is investigated *via* degradation measurement in the presence of scavenger of reactive species and PL spectra of catalysts. Photodegradation experiments of methyl orange and methylene blue confirm the wide applicability of the catalyst. It is deduced to be attributed to the synergistic effects of the following factors: firstly, the rapid Fenton oxidation brings about massive defects in PPy layer, thereby strongly improves its adsorption to RhB; secondly, the *in situ* dissolved Fe^{3+} is also reduced to Fe^{2+} and embedded into the PPy layer through N–Fe coordination thus improves the activity in Fenton reaction; thirdly, the presence of PPy coating layer prevents the agglomeration of magnetic particles; the last but the most important, the PPy layer on $CoFe_2O_4$ enhances the absorption of light, inhibits the combination of photo-generated charge carriers and promotes the electron transfer for H_2O_2 decomposition.

Conflicts of interest

There are no conflicts to declare.

Notes and references

1 Y. Zhang, Z. Chen, L. Zhou, P. Wu, Y. Zhao, Y. Lai and F. Wang, Heterogeneous Fenton degradation of bisphenol A using Fe_3O_4@β-CD/rGO composite: synergistic effect, principle and way of degradation, *Environ. Pollut.*, 2019, **244**, 93–101.

2 A. Al-Anazi, W. H. Abdelraheem, C. Han, M. N. Nadagouda, L. Sygellou, M. K. Arfanis, P. Falaras, V. K. Sharma and D. D. Dionysiou, Cobalt ferrite nanoparticles with controlled composition-peroxymonosulfate mediated degradation of 2-phenylbenzimidazole-5-sulfonic acid, *Appl. Catal., B*, 2018, **221**, 266–279.

3 Y. Yao, Y. Cai, F. Lu, F. Wei, X. Wang and S. Wang, Magnetic recoverable $MnFe_2O_4$ and $MnFe_2O_4$-graphene hybrid as heterogeneous catalysts of peroxymonosulfate activation for efficient degradation of aqueous organic pollutants, *J. Hazard. Mater.*, 2014, **270**, 61–70.

4 C. Ding, S. Xiao, Y. Lin, P. Yu, M.-e. Zhong, L. Yang, H. Wang, L. Su, C. Liao and Y. Zhou, Attapulgite-supported nano-Fe^0/ peroxymonsulfate for quinclorac removal: performance, mechanism and degradation pathway, *Chem. Eng. J.*, 2019, **360**, 104–114.

5 K. Zhu, C. Jin, Z. Klencsár, A. Ganeshraja and J. Wang, Cobalt–iron oxide, alloy and nitride: synthesis, characterization and application in catalytic peroxymonosulfate activation for orange II degradation, *Catalysts*, 2017, **7**, 138.

6 H. Sun, X. Yang, L. Zhao, T. Xu and J. Lian, One-pot hydrothermal synthesis of octahedral $CoFe/CoFe_2O_4$ submicron composite as heterogeneous catalysts with enhanced peroxymonosulfate activity, *J. Mater. Chem. A*, 2016, **4**, 9455–9465.

7 X. Li, Y. Liu, J. Deng, S. Xie, X. Zhao, Y. Zhang, K. Zhang, H. Arandiyan, G. Guo and H. Dai, Enhanced catalytic performance for methane combustion of 3DOM $CoFe_2O_4$ by co-loading MnO_x and Pd–Pt alloy nanoparticles, *Appl. Surf. Sci.*, 2017, **403**, 590–600.

8 Y. Popat, M. Orlandi, N. Patel, R. Edla, N. Bazzanella, S. Gupta, M. Yadav, S. Pillai, M. Patel and A. Miotello, Pulsed laser deposition of $CoFe_2O_4/CoO$ hierarchical-type nanostructured heterojuction forming a Z-scheme for efficient spatial separation of photoinduced electron-hole pairs and highly active surface area, *Appl. Surf. Sci.*, 2019, **489**, 584–594.

9 Y. Yao, J. Qin, H. Chen, F. Wei, X. Liu, J. Wang and S. Wang, One-pot approach for synthesis of N-doped $TiO_2/ZnFe_2O_4$ hybrid as an efficient photocatalyst for degradation of aqueous organic pollutants, *J. Hazard. Mater.*, 2015, **291**, 28–37.

10 H. Zhou, X. Yue, H. Lv, L. Kong, Z. Ji and X. Shen, Graphene oxide-$FePO_4$ nanocomposite: synthesis, characterization and photocatalytic properties as a Fenton-like catalyst, *Ceram. Int.*, 2018, **44**, 7240–7244.

11 A. Kalam, A. G. Al-Sehemi, M. Assiri, G. Du, T. Ahmad, I. Ahmad and M. Pannipara, Modified solvothermal synthesis of cobalt ferrite ($CoFe_2O_4$) magnetic nanoparticles photocatalysts for degradation of methylene blue with H_2O_2/visible light, *Results Phys.*, 2018, **8**, 1046–1053.

12 H.-Y. He and J. Lu, Highly photocatalytic activities of magnetically separable reduced graphene oxide-$CoFe_2O_4$ hybrid nanostructures in dye photodegradation, *Sep. Purif. Technol.*, 2017, **172**, 374–381.

13 S. Peng, L. Li, Y. Hu, M. Srinivasan, F. Cheng, J. Chen and S. Ramakrishna, Fabrication of spinel one-dimensional architectures by single-spinneret electrospinning for energy storage applications, *ACS Nano*, 2015, **9**, 1945–1954.

14 B. Cai, M. Zhao, Y. Ma, Z. Ye and J. Huang, Bioinspired formation of 3D hierarchical $CoFe_2O_4$ porous microspheres for magnetic-controlled drug release, *ACS Appl. Mater. Interfaces*, 2015, **7**, 1327–1333.

15 K. Zhu, C. Jin, C. Zhao, R. Hu, Z. Klencsar, G. A. Sundaram, D. F. Srankó, R. Ge and J. Wang, Modulation synthesis of multi-shelled cobalt-iron oxides as efficient catalysts for peroxymonosulfate-mediated organics degradation, *Chem. Eng. J.*, 2019, **359**, 1537–1549.

16 C. Wang, H. Su, Y. Ma, D. Yang, Y. Dong, D. Li, L. Wang, Y. Liu and J. Zhang, Coordination polymers-derived three-dimensional hierarchical $CoFe_2O_4$ hollow spheres as high-performance lithium ion storage, *ACS Appl. Mater. Interfaces*, 2018, **10**, 28679–28685.

17 L. Xu, W. Chu and L. Gan, Environmental application of graphene-based $CoFe_2O_4$ as an activator of peroxymonosulfate for the degradation of a plasticizer, *Chem. Eng. J.*, 2015, **263**, 435–443.

18 Q. Yang, H. Choi, S. R. Al-Abed and D. D. Dionysiou, Iron–cobalt mixed oxide nanocatalysts: heterogeneous peroxymonosulfate activation, cobalt leaching, and ferromagnetic properties for environmental applications, *Appl. Catal., B*, 2009, **88**, 462–469.

19 K. Zhang, W. Zuo, Z. Wang, J. Liu, T. Li, B. Wang and Z. Yang, A simple route to $CoFe_2O_4$ nanoparticles with shape and size control and their tunable peroxidase-like activity, *RSC Adv.*, 2015, **5**, 10632–10640.

20 G. S. Parkinson, Iron oxide surfaces, *Surf. Sci. Rep.*, 2016, **71**, 272–365.

21 C. R. Vestal and Z. J. Zhang, Synthesis and magnetic characterization of Mn and Co spinel ferrite-silica nanoparticles with tunable magnetic core, *Nano Lett.*, 2003, **3**, 1739–1743.

22 Y. Guo, Y. Tao, X. Ma, J. Jin, S. Wen, W. Ji, W. Song, B. Zhao and Y. Ozaki, A dual colorimetric and SERS detection of Hg^{2+} based on the stimulus of intrinsic oxidase-like catalytic activity of Ag-$CoFe_2O_4$/reduced graphene oxide nanocomposites, *Chem. Eng. J.*, 2018, **350**, 120–130.

23 Z. Zhang, Y. Jiang, M. Chi, Z. Yang, G. Nie, X. Lu and C. Wang, Fabrication of Au nanoparticles supported on $CoFe_2O_4$ nanotubes by polyaniline assisted self-assembly strategy and their magnetically recoverable catalytic properties, *Appl. Surf. Sci.*, 2016, **363**, 578–585.

24 S. Akbayrak, M. Kaya, M. Volkan and S. Özkar, Palladium(0) nanoparticles supported on silica-coated cobalt ferrite: a highly active, magnetically isolable and reusable catalyst for hydrolytic dehydrogenation of ammonia borane, *Appl. Catal., B*, 2014, **147**, 387–393.

25 M. Kaya, M. Zahmakiran, S. Özkar and M. r. Volkan, Copper(0) nanoparticles supported on silica-coated cobalt ferrite magnetic particles: cost effective catalyst in the hydrolysis of ammonia-borane with an exceptional reusability performance, *ACS Appl. Mater. Interfaces*, 2012, **4**, 3866–3873.

26 X. Li, H. Lu, Y. Zhang and F. He, Efficient removal of organic pollutants from aqueous media using newly synthesized polypyrrole/CNTs-$CoFe_2O_4$ magnetic nanocomposites, *Chem. Eng. J.*, 2017, **316**, 893–902.

27 S. Ma, S. Zhan, Y. Jia and Q. Zhou, Highly efficient antibacterial and Pb(II) removal effects of Ag-$CoFe_2O_4$-GO nanocomposite, *ACS Appl. Mater. Interfaces*, 2015, **7**, 10576–10586.

28 S. Bai, X. Shen, X. Zhong, Y. Liu, G. Zhu, X. Xu and K. Chen, One-pot solvothermal preparation of magnetic reduced graphene oxide-ferrite hybrids for organic dye removal, *Carbon*, 2012, **50**, 2337–2346.

29 C. Liu, L. Liu, X. Tian, Y. Wang, R. Li, Y. Zhang, Z. Song, B. Xu, W. Chu and F. Qi, Coupling metal–organic frameworks and g-C_3N_4 to derive Fe@N-doped graphene-like carbon for peroxymonosulfate activation: Upgrading framework stability and performance, *Appl. Catal., B*, 2019, **255**, 117763.

30 Y. Yao, F. Lu, Y. Zhu, F. Wei, X. Liu, C. Lian and S. Wang, Magnetic core–shell $CuFe_2O_4@C_3N_4$ hybrids for visible light photocatalysis of Orange II, *J. Hazard. Mater.*, 2015, **297**, 224–233.

31 F. Wu, J. Chen, R. Chen, S. Wu, L. Li, S. Chen and T. Zhao, Sulfur/polythiophene with a core/shell structure: synthesis and electrochemical properties of the cathode for rechargeable lithium batteries, *J. Phys. Chem. C*, 2011, **115**, 6057–6063.

32 L. Wang, X. Feng, L. Ren, Q. Piao, J. Zhong, Y. Wang, H. Li, Y. Chen and B. Wang, Flexible solid-state supercapacitor based on a metal–organic framework interwoven by electrochemically-deposited PANI, *J. Am. Chem. Soc.*, 2015, **137**, 4920–4923.

33 S. Sambaza, A. Maity and K. Pillay, Enhanced degradation of BPA in water by PANI supported Ag/TiO_2 nanocomposite under UV and visible light, *J. Environ. Chem. Eng.*, 2019, **7**, 102880.

34 F. Su, C. K. Poh, J. S. Chen, G. Xu, D. Wang, Q. Li, J. Lin and X. W. Lou, Nitrogen-containing microporous carbon nanospheres with improved capacitive properties, *Energy Environ. Sci.*, 2011, **4**, 717–724.

35 H. Tang, J. Wang, H. Yin, H. Zhao, D. Wang and Z. Tang, Growth of polypyrrole ultrathin films on MoS_2 monolayers as high-performance supercapacitor electrodes, *Adv. Mater.*, 2015, **27**, 1117–1123.

36 S. Ghosh, N. A. Kouamé, L. Ramos, S. Remita, A. Dazzi, A. Deniset-Besseau, P. Beaunier, F. Goubard, P.-H. Aubert and H. Remita, Conducting polymer nanostructures for photocatalysis under visible light, *Nat. Mater.*, 2015, **14**, 505.

37 X. Yuan, D. Floresyona, P.-H. Aubert, T.-T. Bui, S. Remita, S. Ghosh, F. Brisset, F. Goubard and H. Remita, Photocatalytic degradation of organic pollutant with polypyrrole nanostructures under UV and visible light, *Appl. Catal., B*, 2019, **242**, 284–292.

38 J. Xu, Y. Hu, C. Zeng, Y. Zhang and H. Huang, Polypyrrole decorated BiOI nanosheets: Efficient photocatalytic activity for treating diverse contaminants and the critical role of bifunctional polypyrrole, *J. Colloid Interface Sci.*, 2017, **505**, 719–727.

39 K. R. Reddy, M. Hassan and V. G. Gomes, Hybrid nanostructures based on titanium dioxide for enhanced photocatalysis, *Appl. Catal., A*, 2015, **489**, 1–16.

40 T. Yao, T. Cui, H. Wang, L. Xu, F. Cui and J. Wu, A simple way to prepare $Au@polypyrrole/Fe_3O_4$ hollow capsules with high stability and their application in catalytic reduction of methylene blue dye, *Nanoscale*, 2014, **6**, 7666–7674.

41 Y. Tao, E. Ju, J. Ren and X. Qu, Polypyrrole nanoparticles as promising enzyme mimics for sensitive hydrogen peroxide detection, *Chem. Commun.*, 2014, **50**, 3030–3032.

42 Z. Yang, C. Zhang, J. Zhang and W. Bai, Potentiometric glucose biosensor based on core–shell Fe_3O_4–enzyme–polypyrrole nanoparticles, *Biosens. Bioelectron.*, 2014, **51**, 268–273.

43 N. Ballav, R. Das, S. Giri, A. M. Muliwa, K. Pillay and A. Maity, L-cysteine doped polypyrrole (PPy@L-Cyst): a super adsorbent for the rapid removal of Hg^{+2} and efficient catalytic activity of the spent adsorbent for reuse, *Chem. Eng. J.*, 2018, **345**, 621–630.

44 L. W. Zhang, H. B. Fu and Y. F. Zhu, Efficient TiO_2 photocatalysts from surface hybridization of TiO_2 particles with graphite-like carbon, *Adv. Funct. Mater.*, 2008, **18**, 2180–2189.

45 G. Wang, Y. Ma, Z. Wei and M. Qi, Development of multifunctional cobalt ferrite/graphene oxide nanocomposites for magnetic resonance imaging and controlled drug delivery, *Chem. Eng. J.*, 2016, **289**, 150–160.

46 R. Das, V. S. Sypu, H. K. Paumo, M. Bhaumik, V. Maharaj and A. Maity, Silver decorated magnetic nanocomposite ($Fe_3O_4@PPy-MAA/Ag$) as highly active catalyst towards reduction of 4-nitrophenol and toxic organic dyes, *Appl. Catal., B*, 2019, **244**, 546–558.

47 S. Zhang, K. Zhu, G. Lv, G. Wang, D. Yu and J. Shao, UV-catalytic preparation of polypyrrole nanoparticles induced by H_2O_2, *J. Phys. Chem. C*, 2015, **119**, 18707–18718.

48 M. Kamranifar, A. Allahresani and A. Naghizadeh, Synthesis and characterizations of a novel $CoFe_2O_4@CuS$ magnetic nanocomposite and investigation of its efficiency for photocatalytic degradation of penicillin G antibiotic in simulated wastewater, *J. Hazard. Mater.*, 2019, **366**, 545–555.

49 S. Bose, T. Kuila, M. E. Uddin, N. H. Kim, A. K. Lau and J. H. Lee, In-situ synthesis and characterization of electrically conductive polypyrrole/graphene nanocomposites, *Polymer*, 2010, **51**, 5921–5928.

50 N. Li, Z. Ji, L. Chen, X. Shen, Y. Zhang, S. Cheng and H. Zhou, Anchoring of Ag nanoparticles on Fe_3O_4 modified polydopamine sub-micrometer spheres with enhanced catalytic activity, *Appl. Surf. Sci.*, 2018, **462**, 1–7.

51 S. Xiong, S. Ye, X. Hu and F. Xie, Electrochemical detection of ultra-trace Cu (II) and interaction mechanism analysis between amine-groups functionalized $CoFe_2O_4$/reduced graphene oxide composites and metal ion, *Electrochim. Acta*, 2016, **217**, 24–33.

52 T. Yao, W. Jia, Y. Feng, J. Zhang, Y. Lian, J. Wu and X. Zhang, Preparation of reduced graphene oxide nanosheet/Fe_xO_y/nitrogen-doped carbon layer aerogel as photo-Fenton catalyst with enhanced degradation activity and reusability, *J. Hazard. Mater.*, 2019, **362**, 62–71.

53 W. WP., H. Yang, T. Xian and J. JL, XPS and magnetic properties of $CoFe_2O_4$ nanoparticles synthesized by a polyacrylamide gel route, *Mater. Trans.*, 2012, **53**, 1586–1589.

54 T. Yamashita and P. Hayes, Analysis of XPS spectra of Fe^{2+} and Fe^{3+} ions in oxide materials, *Appl. Surf. Sci.*, 2008, **254**, 2441–2449.

55 C. Dong, J. Lu, B. Qiu, B. Shen, M. Xing and J. Zhang, Developing stretchable and graphene-oxide-based hydrogel for the removal of organic pollutants and metal ions, *Appl. Catal., B*, 2018, **222**, 146–156.

56 X. Zhang, S. Yu, Y. Liu, Q. Zhang and Y. Zhou, Photoreduction of non-noble metal Bi on the surface of Bi_2WO_6 for enhanced visible light photocatalysis, *Appl. Surf. Sci.*, 2017, **396**, 652–658.

57 J. Liqiang, Q. Yichun, W. Baiqi, L. Shudan, J. Baojiang, Y. Libin, F. Wei, F. Honggang and S. Jiazhong, Review of photoluminescence performance of nano-sized semiconductor materials and its relationships with photocatalytic activity, *Sol. Energy Mater. Sol. Cells*, 2006, **90**, 1773–1787.

58 Y. Sun, N. G. Ndifor-Angwafor, D. J. Riley and M. N. Ashfold, Synthesis and photoluminescence of ultra-thin ZnO nanowire/nanotube arrays formed by hydrothermal growth, *Chem. Phys. Lett.*, 2006, **431**, 352–357.

59 T. Guo, K. Wang, G. Zhang and X. Wu, A novel α-Fe_2O_3@g-C_3N_4 catalyst: synthesis derived from Fe-based MOF and its superior photo-Fenton performance, *Appl. Surf. Sci.*, 2019, **469**, 331–339.

60 J. Li, C. Xiao, K. Wang, Y. Li and G. Zhang, Enhanced Generation of Reactive Oxygen Species under Visible Light Irradiation by Adjusting the Exposed Facet of $FeWO_4$ Nanosheets To Activate Oxalic Acid for Organic Pollutant Removal and Cr(VI) Reduction, *Environ. Sci. Technol.*, 2019, **53**, 11023–11030.

61 N. Zhang, X. Li, H. Ye, S. Chen, H. Ju, D. Liu, Y. Lin, W. Ye, C. Wang and Q. Xu, Oxide defect engineering enables to couple solar energy into oxygen activation, *J. Am. Chem. Soc.*, 2016, **138**, 8928–8935.

62 M. Ma, Y. Yang, W. Li, Y. Ma, Z. Tong, W. Huang, L. Chen, G. Wu, H. Wang and P. Lyu, Synthesis of yolk-shell structure Fe_3O_4/P(MAA-MBAA)-PPy/Au/void/TiO_2 magnetic microspheres as visible light active photocatalyst for degradation of organic pollutants, *J. Alloys Compd.*, 2019, **810**, 151807.

63 L. Bian, Y. Liu, G. Zhu, C. Yan, J. Zhang and A. Yuan, Ag@$CoFe_2O_4$/Fe_2O_3 nanorod arrays on carbon fiber cloth as SERS substrate and photo-Fenton catalyst for detection and degradation of R6G, *Ceram. Int.*, 2018, **44**, 7580–7587.

64 H. Y. He and J. Lu, Highly photocatalytic activities of magnetically separable reduced graphene oxide-$CoFe_2O_4$ hybrid nanostructures in dye photodegradation, *Sep. Purif. Technol.*, 2017, **172**, 374–381.

65 X. Tong, W. Jia, Y. Li, T. Yao, J. Wu and M. Yang, One-step preparation of reduced graphene oxide/Prussian blue/polypyrrole aerogel and their enhanced photo-Fenton performance, *J. Taiwan Inst. Chem. Eng.*, 2019, **102**, 92–98.

66 T. Yao, W. Jia, Y. Feng, J. Zhang, Y. Lian, J. Wu and X. Zhang, Preparation of reduced graphene oxide nanosheet/Fe_xO_y/nitrogen-doped carbon layer aerogel as photo-Fenton catalyst with enhanced degradation activity and reusability, *J. Hazard. Mater.*, 2019, **362**, 62–71.

67 M. Fatma, M. R. Abukhadra and S. Mohamed, Removal of safranin dye from water using polypyrrole nanofiber/Zn-Fe layered double hydroxide nanocomposite (Ppy NF/Zn-Fe LDH) of enhanced adsorption and photocatalytic properties, *Sci. Total Environ.*, 2018, **640–641**, 352–363.

68 H. Deng, X. Li, Q. Peng, X. Wang, J. Chen and Y. Li, Monodisperse magnetic single-crystal ferrite microspheres, *Angew. Chem.*, 2005, **117**, 2842–2845.